RESEARCH ARTICLE

Key Points:
- Surface circulation patterns under varying wind conditions during open water seasons in the northeastern Chukchi Sea are defined
- Northeasterly winds with magnitudes greater than 6 m s^{-1} reverse the northeastward-flowing coastal current to the southwest
- A transitional current pattern during the onset of high magnitude northeasterly winds is described

Supporting Information:
- Supporting Information S1

Correspondence to:
Y.-C. Fang,
yfang2@alaska.edu

Surface Current Patterns in the Northeastern Chukchi Sea and Their Response to Wind Forcing

Ying-Chih Fang[1] (ID), Rachel A. Potter[1], Hank Statscewich[1], Thomas J. Weingartner[1] (ID), Peter Winsor[1], and Brita K. Irving[1]

[1]College of Fisheries and Ocean Sciences, University of Alaska Fairbanks, Fairbanks, AK, USA

Abstract We measured northeastern Chukchi Sea surface currents using high-frequency radar systems (HFR) during the ice-free periods of August to October from 2010–2014. We analyzed these data, along with regional winds, using Self-Organizing Maps (SOM) to develop a set of surface current-wind patterns. Temporal changes in the SOM patterns consist predominantly of two patterns comprising northeastward and southwestward surface currents. A third pattern represents a transitional stage established during the onset of strong northeasterly winds. These patterns are analogous to the first two eigenmodes of an empirical orthogonal function analysis of the HFR data. The first principal component (PC1) is significantly correlated ($\sim$0.8) to that of the winds and is directly related to the time series of SOM-derived patterns. The sign of PC1 changes when the speed of local northeasterly winds exceeds $\sim$6 m s^{-1}, at which point the northeastward surface currents reverse to the southwest. This finding agrees with previous models and observations that suggest this wind threshold is needed to overcome the pressure gradient between the Pacific and Arctic Oceans. The transitional stage is characterized by alongshore currents bifurcating in the vicinity of Icy Cape and wind-driven Ekman currents north of 71.5°N. Its development is a manifestation of interactions among the poleward pressure gradient, wind stress, and geostrophic flow due to the coastal setdown.

1. Introduction

The Chukchi Sea is the gateway between the Pacific and Arctic Oceans. This vast marginal sea, though shallow in depth ($\sim$50 m), is prominent in shaping the thermohaline structure and freshwater budget of the western Arctic Ocean. The annual mean transport of Pacific water into the Chukchi Sea through Bering Strait is $\sim$0.8 Sv (Roach et al., 1995; Woodgate et al., 2005) and was more recently reported as $\sim$1.1 Sv (Woodgate et al., 2012), resulting in a poleward flux of heat and freshwater that affects sea ice distributions (Shimada et al., 2006; Steele et al., 2008; Wood et al., 2015; Woodgate et al., 2006) and supplies $\sim$30% of the freshwater input to the Arctic Ocean (Serreze et al., 2006). Although the northward transport is forced by the steric height difference between the Bering Sea and Arctic Ocean due to interbasin salinity differences (Aagaard et al., 2006; Stigebrandt, 1984), the flow field varies due to atmospheric forcing (Danielson et al., 2014; Woodgate et al., 2012).

As Pacific waters flow northward through Bering Strait and across the Chukchi Sea, observations (Paquette & Bourke, 1981; Pickart et al., 2010, 2016; Weingartner et al., 1998, 2005, 2013a; Woodgate et al., 2005) and numerical models (Spall, 2007; Winsor & Chapman, 2004) indicate that the throughflow is bathymetrically steered along three major pathways (Figure 1). One branch follows Hope Valley and flows northward through Herald Canyon; another flows through the Central Channel between Herald and Hanna Shoals; and the third flows along the Alaskan coast and into Barrow Canyon where it becomes swift ($\sim$50 cm s^{-1}) and narrow ($\sim$40 km) (Gong & Pickart, 2015; Itoh et al., 2013; Spall, 2007; Weingartner et al., 2017b; Winsor & Chapman, 2004). During summer and early fall, the coastal branch includes buoyant, nutrient poor Alaskan Coastal Water, carried by the Alaskan Coastal Current (ACC) (Paquette & Bourke, 1974). Itoh et al. (2013) used long-term mooring observations at the mouth of Barrow Canyon and found the greatest heat and freshwater fluxes occur from August to October.

Owing to the shallowness of the Chukchi shelf, wind forcing substantially influences the circulation pathways. On average, each branch flows poleward, whereas the mean wind field over the Chukchi shelf is from
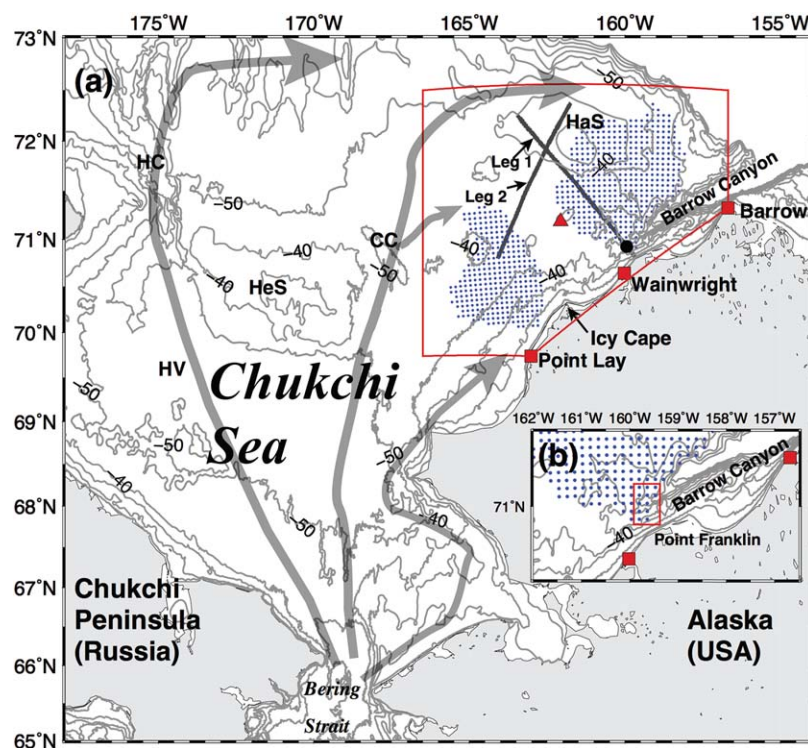
Figure 1. (a) Map of the Chukchi Sea with place names. Blue dots indicate 2012 HFR network grid points with more than 60% temporal coverage. Red squares show locations of HFR field sites. The red outlined area represents the NARR wind domain used in the SOM and EOF analysis, with the red triangle the location representative of the shelf wind time series. Legs 1 and 2 are hydrographic transects conducted in September 2013. Black dot north of Wainwright denotes the BC2 mooring. Gray arrows show schematic pathways of Pacific waters. Bathymetric contours are drawn from 10 to 100 m at 10 m intervals. Place names include HV = Hope Valley, HC = Herald Canyon, HeS = Herald Shoal, CC = Central Channel, and HaS = Hanna Shoal. (b) Grid points within the red rectangle are used to determine upcanyon and downcanyon flow conditions.

the east-northeast (Weingartner et al., 2013a) and opposes the mean flow. Local winds are highly correlated with the flow field on the Chukchi shelf (Itoh et al., 2013; Weingartner et al., 2005), except in Herald Canyon (Woodgate et al., 2005). Winsor and Chapman (2004) used a barotropic model to examine the sensitivity of shelf flow under changing winds and found that when northeasterly winds exceeded ~6 m s^{-1}, the coastal current near Barrow reversed to the southwest. Similar reversals were observed using subsurface moorings and ship-borne surveys (Aagaard & Roach, 1990; Hirano et al., 2016; Johnson, 1989; Mountain et al., 1976; Okkonen et al., 2009; Weingartner et al., 1998); however, subsurface measurements do not capture the upper few meters and so may not be representative of the surface current field. Therefore, surface current observations are essential to evaluate the flow imposed by wind forcing, especially when considering the potential transport of surface-trapped dissolved and suspended materials. In particular, surface currents may be important in the distribution of fish larvae (Geoffroy et al., 2016; Wyllie-Echeverria et al., 1992) and zooplankton (Questel et al., 2013).

This study focuses on synoptic surface current measurements collected in the northeastern Chukchi Sea using shore-based high-frequency radar systems (HFR) deployed along the Alaskan coast in the villages of Barrow, Wainwright, and Point Lay during the open-water seasons of 2010–2014 (Figure 1). The HFR measurements have a resolution of 6 km and a range of ~150 km from the coast. We investigate the relationship between surface currents and winds using Self-Organizing Maps (SOM; Kohonen, 2001) to extract surface current patterns paired with wind fields.

The paper is arranged as follows. The HFR and North American Regional Reanalysis (NARR) data acquisition and processing are discussed in section 2, followed by an overview and methodology of the SOM analysis. Section 3 presents the SOM-derived patterns, including their temporal evolutions in response to the winds.

Surface current patterns from conventional empirical orthogonal function (EOF) analysis are also discussed. These results, along with mean circulation patterns, spatial correlations, and hydrographic observations, suggest differing dynamical environments north and south of ~71.5°N. Section 4 discusses the results with the aid of the regional hydrographic setting, and section 5 summarizes the paper.

2. Data and Methods

2.1. Surface Currents

A three-HFR network monitored surface currents (~2 m depth; Stewart & Joy, 1974) in the northeastern Chukchi Sea (Figure 1a) using 5 MHz SeaSonde systems. This frequency requires the presence of surface gravity waves with wavelengths of ~30 m (Barrick, 1978; Paduan & Washburn, 2013) and thus sufficient ice-free waters and winds to generate such waves. The SeaSonde records the reflected Bragg scatter from the waves, after which, assuming deep-water wave theory, one uses the Doppler-shifted radar return to calculate surface current speeds advancing toward or retreating from the radar. The HFR network presented herein is unique in that it is operated in a polar environment where waters are ice-covered ~8 months of the year. Sea ice presence varies from year-to-year and contaminates the radar signals. Therefore, we only considered the time period from 1 August to 31 October of each year, when little or no sea ice was present within the radar mask. The HFR site locations were dictated by grid power availability, which necessitated that our sites be more broadly separated (~150 km) than optimal (~75 km). Thus, the resultant radar coverage comprises two domains: a southern mask (Point Lay and Wainwright overlap) and a northern mask (Barrow and Wainwright overlap). The coverage leaves a persistent gap along ~162.5°W (Figure 1a). Although data from 2010–2014 were analyzed, we primarily present results from 2012 when spatial coverage was most extensive.

One-dimensional radial surface currents, $\vec{r}$, from each HFR were used to estimate two-dimensional surface currents, $\vec{u}$, following the optimal interpolation (OI) scheme of Kim et al. (2007, 2008). Fang et al. (2015) investigated the performance of the OI method applied to the Chukchi HFR network. They used analytical stream functions to simulate spatially and temporally varying currents and found that for derived $\vec{u}$ with a normalized skill ≥ 0.7 (0–1 scale), errors were ~2° angle shift and <0.1% magnitude variation. They found that the most important quality control factor for the estimated $\vec{u}$ is the contribution of radial velocities from different HFR, which is defined as the ratio of overlapping $\vec{r}$ (ROR). The higher the ROR, the more biased the estimate of $\vec{u}$, by as much as ~20° in angle shift with a corresponding ~6% change in magnitude.

The $\vec{u}$ were computed every cardinal hour, and the ROR at each grid point was determined. Fang et al. (2015) show that areas with ≥ 0.7 skill closely coincide to those with ROR < ~5, thus grid points with ROR $\geq$ 5 were discarded. In addition, if the number of contributing $\vec{r}$ in the search radius (35 km) of the grid point was <20, the OI-output $\vec{u}$ at the grid point was flagged. The threshold 20 was used to prevent $\vec{u}$ from being calculated using a small number of $\vec{r}$, which can result in erroneous current estimates. For the OI scheme we employed criterion based on the cosine angle of paired $\vec{r}$ (Chavanne et al., 2007) to avoid estimates along the radar baseline where $\vec{u}$ cannot be properly resolved. If the angle between paired $\vec{r}$ was not between 30° and 120°, the grid point was excluded from the analysis. This range was chosen in conjunction with other quality control factors reported in Fang et al. (2015) to allow optimal determination of $\vec{u}$.

Data gaps can degrade filtering quality and cause spectral leakage that dampens filtered results, so after some experimentation, gaps in the $\vec{u}$ time series for each year were filled with zeros following Chavanne et al. (2007). Grid points containing $\geq 60\%$ temporal coverage (Figure 1a) were then filtered with a ninth-order 40 h cutoff low-pass Butterworth filter to remove high frequency signals (tidal and inertial motions).

2.2. Winds

Wind velocities were extracted from the NARR 10 m surface field (Mesinger et al., 2006), at ~35 km grid-spacing every 3 h, for the same period as the HFR data and then linearly interpolated to hourly intervals and filtered as described above. Quantitative comparisons between the NARR winds and those measured at the Barrow and Wainwright airports were conducted in Weingartner et al. (2013b), who determined that NARR winds are a reliable proxy for observed winds. A domain covering the radar mask (Figure 1a) is used

for the SOM and EOF analyses with 162.1°W, 71.2°N (red triangle in Figure 1a) chosen as representative of winds in the study area.

2.3. SOM Analysis

SOM is a tool capable of capturing detailed synoptic variability in a data set through time with multiple variables. Richardson et al. (2003) and Liu and Weisberg (2005) provide excellent background on the application of SOM to oceanographic data. Liu et al. (2006) investigated SOM sensitivities to varying parameter choices and discussed its performance compared with EOF analysis. Ideally, the major circulation features derived from both methods should be consistent with one another. However, Liu et al. (2006) showed that EOFs failed to extract predefined patterns from synthetic data, whereas SOM completed the task perfectly. The advantage of using SOM, a nonlinear approach, compared with EOFs for HFR currents is the capability to extract detailed patterns from synoptic data sets (Mau et al., 2007) and to identify when they occur in time. As will be shown, higher-order EOF eigenmodes may not correctly capture complicated patterns.

We used the SOM Toolbox for our analysis (http://www.cis.hut.fi/somtoolbox/; v. 2.0) and followed the parameters discussed in Liu et al. (2006). As shown by Liu et al. (2007), Mihanović et al. (2011), and Vilibić et al. (2016), SOM is capable of incorporating two different data sets (e.g., HFR and wind data) to resolve associated patterns. Gap-filling approaches have been developed for HFR data (Fredj et al., 2016; Kaplan & Lekien, 2007), but these tend to produce spurious results during periods of sparse data returns. Therefore, we replace HFR data gaps with zeros rather than using gap-filling approaches. This procedure makes the linear initialization of SOM numerically valid, so that the first two eigenmodes of the data matrix can be determined (Kohonen, 2001). Beckers and Rixen (2003) found that introducing zeros into the raw data matrix can increase the variance of dominant modes and reduce errant interpolations.

The resultant number of patterns produced by SOM has to be chosen a priori and is subjective. The larger this number, the more temporal variability will be extracted from the data, while a smaller number of patterns tends to compress information yielding less temporal variability (Liu et al., 2006). After experimentation, we found that twelve patterns are optimal for our data in that unique circulation features and data gaps can be isolated.

Twelve patterns were derived each year for 2010–2014. Although winds, radar coverage, and data gaps differed from year-to-year, we were able to categorize similar patterns into four major flow regimes (see section 3.1). SOM patterns were visually confirmed with the data time series in each year to verify SOM performance. There was a pattern in all years made up of weak or negligible currents. We show that this weak current pattern correlates with a decrease in data returns (see section 3.2) and can be treated as an error analog that facilitates our interpretation of resultant time series.

2.4. EOF Analysis

EOF analysis provides another perspective of surface current responses to winds. We will show that the first eigenmode and its principal component (PC1) corroborate the SOM-derived patterns. Due to data gaps, a direct EOF computation for $\vec{u}$ was not possible; therefore, a field reconstructed approach called data interpolating empirical orthogonal functions (DINEOF) (Beckers & Rixen, 2003; Taylor et al., 2013) was used to fill data gaps. (In August 2010 and 2013, there were too many $\vec{u}$ gaps for effective use of the DINEOF approach, so the 1 September to 31 October period was used.) Reconstructed $\vec{u}$ and wind time series for each year were then used individually for the EOF analysis following Kaihatu et al. (1998), resulting in two covariance matrices per year. Each EOF analysis yielded a corresponding PC, which we used to diagnose the flow fields. The resultant eigenvalue spectrum was evaluated according to North's significance test (North et al., 1982).

2.5. Hydrography

We used temperature and salinity data collected by a SeaBird 49 FastCAT CTD housed in a towed Acrobat system to highlight different hydrographic environments north and south of ∼71.5°N. One transect started from the western flank of Hanna Shoal and ran southeastward for ∼200 km to offshore Point Franklin, while a second began west of Wainwright near ∼164°W and ran ∼200 km northeastward to the northern edge of Hanna Shoal (Figure 1a). The Acrobat-CTD sampled water depths of up to ∼45 m with horizontal and vertical resolutions of ∼250 and ∼0.5 m, respectively. Details on instrumentation, data acquisition, and processing are given by Martini et al. (2016).

2.6. Subsurface Currents

An ADCP mooring near the head of Barrow Canyon (BC2; nominal 52.3 m depth) monitored transport through Barrow Canyon and was maintained from 2010 to 2015 (Figure 1a). These data allow us to compare flow behaviors throughout the water column. We used hourly time series of estimated along canyon transports following Weingartner et al. (2017b) and vertically averaged velocities to examine subsurface to surface current variations. Data processing of BC2 is found in Weingartner et al. (2017b).

3. Results

3.1. SOM-Derived Patterns

All 12 SOM-derived patterns for 2012 data with paired wind conditions are presented in the supporting information Figure S1and Table S1. To simplify the presentation, we condense the twelve into four representative flow regimes (Figures 2a–2d), along with polar histograms of accompanying wind conditions. The northeastward-flowing regime is the most common pattern (Figure 2a) and defined on the basis of northeastward flow inshore or near the 40 m isobath in the southern mask and in Barrow Canyon in the northern mask. For this regime the flow is coastally intensified with speeds >30 cm s^{-1} in the canyon and within $\sim$70 km of the coast in the southern mask. Currents are weak over the central shelf (<20 cm s^{-1}) and even weaker ($\sim$5 cm s^{-1}) north of 71.5°N. The northeastward-flowing regime occurred $\sim$53% of the time, and $\sim$76% of the winds associated with this pattern have a southerly component. Less than 10% of the winds are northeasterly with wind speeds $<\sim$6 m s^{-1}, suggesting that under these wind conditions the flow is forced primarily by the poleward pressure gradient. Velocity measurements from the BC2 mooring indicate the subsurface flow is also primarily northeastward under these conditions. Coincident southwestward subsurface currents are remnant from flow transitions that have not been fully completed and lag the surface flow. Weingartner et al. (2017b) suggest an adjustment time scale of $\sim$1 day for the vertically-averaged flow in Barrow Canyon.

The second most common circulation feature is the reversal regime (Figure 2b), which occurred $\sim$11% of the time and whose structure is nearly opposite the northeastward-flowing regime. It consists of southwestward flow nearshore and westward flow farther offshore. The wind histogram shows $\sim$60% of the associated winds are northeasterly at >6 m s^{-1} with $\sim$10% of occurrences associated with northerly winds with speeds >6 m s^{-1}. Reversal regime currents are stronger than those for the other circulation patterns, with current speeds >30 cm s^{-1} in Barrow Canyon and inshore of the 40 m isobath offshore of Point Lay. Currents north of 71.5°N and east of Hanna Shoal are also swifter ($\sim$15 cm s^{-1}) for this regime compared to the northeastward-flowing regime. Southwestward surface flow at BC2 predominates during the reversal regime. The occurrence of subsurface northeastward currents during the reversal regime is again due to the adjustment time from surface to depth. This result indicates that, at the head of Barrow Canyon, the flow structure is coherent vertically during the two most common surface circulation patterns but that the vertical shear may be substantial during flow transitions.

The third regime occurred $\sim$16% of the time and is denoted as the northwesterly wind regime (Figure 2c). For this pattern $\sim$90% of the winds are northwesterly, with more than half of the wind events having speeds >6 m s^{-1}. This regime appears to result from interactions between the poleward pressure gradient (northeastward flow) and wind-induced Ekman transport (southward flow). The flow field appears to be spatially variable depending on which driving force dominates. For example, when winds initially shift to the northwesterly quadrant, the resultant Ekman transport may not be large enough to overcome the background pressure gradient. We have found cases where the currents south of 71.5°N are east-northeastward (similar to those seen in the northeastward-flowing regime) but southward north of 71.5°N. This flow pattern develops under evolving northwesterly winds and may last longer than a day. As northwesterly winds persist, the Ekman currents gradually overwhelm the poleward pressure gradient, so that currents are southward at $\sim$10–15 cm s^{-1} over much of the radar mask, with stronger flows ($\sim$20 cm s^{-1}) inshore of the 40 m isobath and southeast of Hanna Shoal.

Subsurface flows observed at BC2 indicate predominately northeastward currents, indicating that the flow was vertically sheared over much of the canyon, except near Point Franklin where the surface flow was still northeastward. This finding implies that the subsurface flow over the central shelf must have been onshore
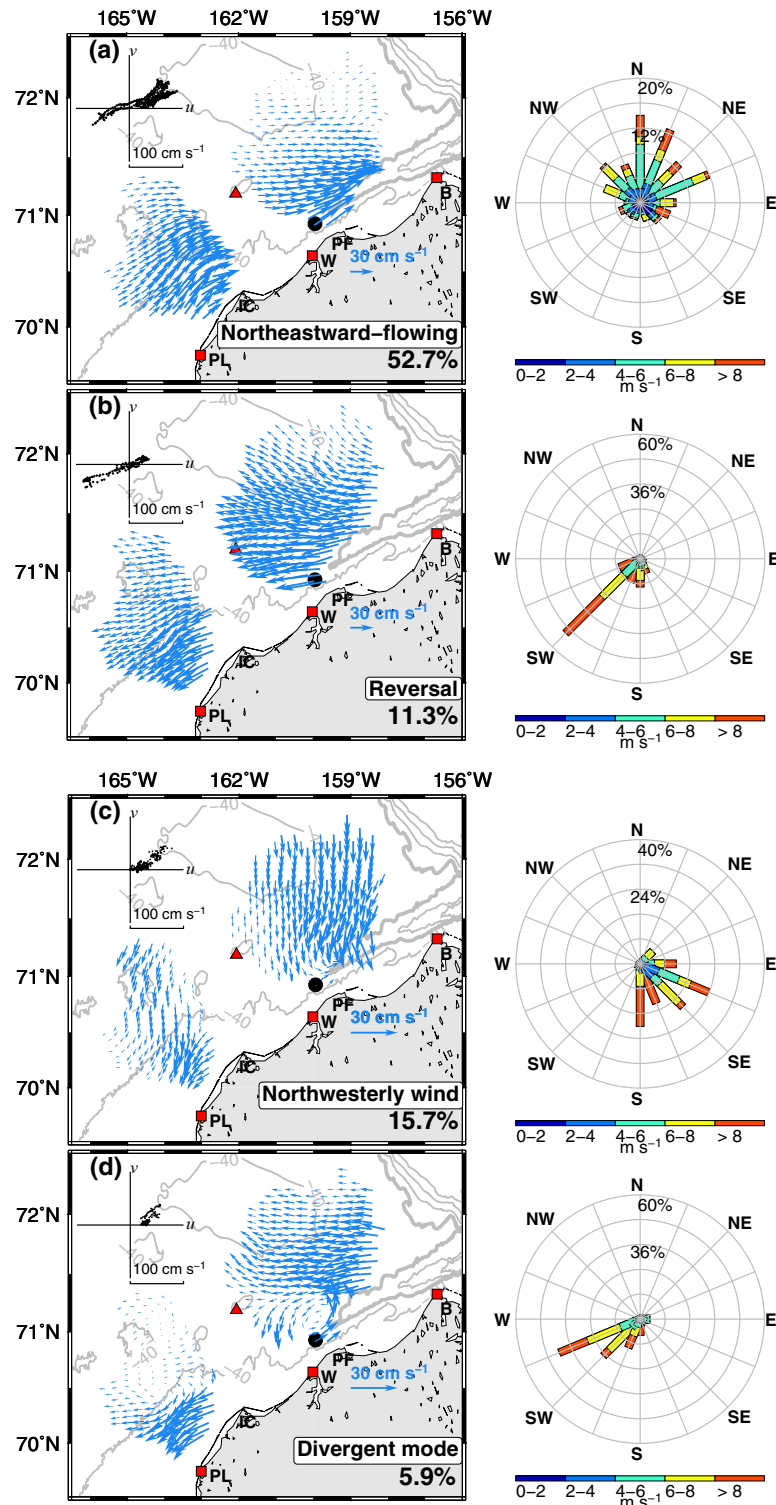
Figure 2. Representative circulation regimes categorized from 12 SOM-derived patterns of surface currents (blue vectors) for 2012: (a) northeastward-flowing regime, (b) reversal regime, (c) Northwesterly wind regime and (d) divergent mode. The frequency of regime occurrence is included in each panel, and the 80 m isobath is thicker to define Barrow Canyon. The inserted scatter plot denotes vertically averaged velocities from mooring BC2 (black dot) when the flow regime occurred. Polar histograms on the right denote wind velocities associated with the flow regime (red triangle). The direction follows oceanographic convention and speed is shaded. The percentage indicates frequencies of winds blowing toward that direction. Note that the scales of current vectors in Figures 2c and 2d are different than those in Figures 2a and 2b.
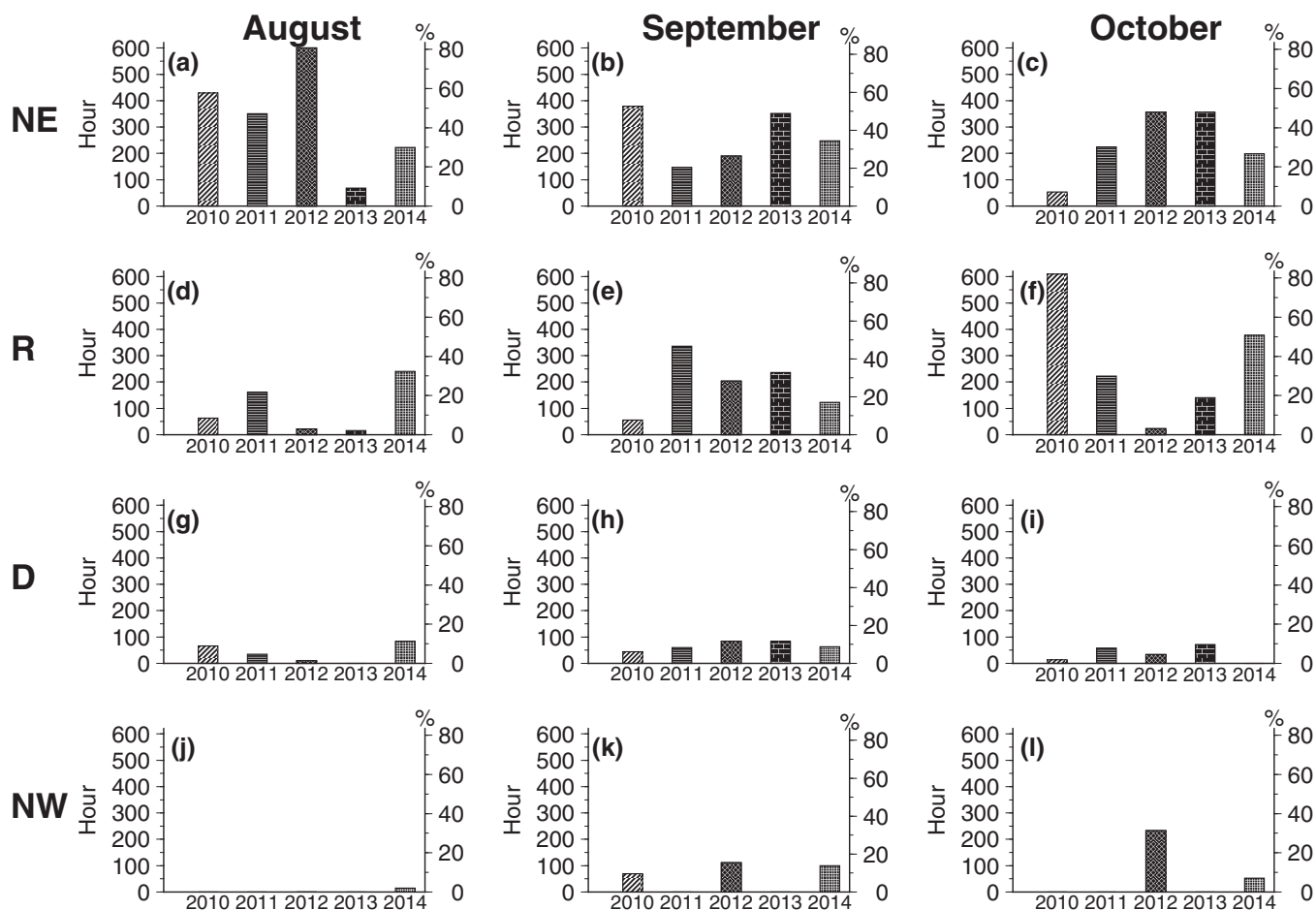
Figure 3. Monthly occurrences of SOM-derived circulation regimes for 2010–2014 with different hatching denoting different years. (a)–(c) Northeastward-flowing regime (NE). (d)–(f) Reversal regime (R). (g)–(i) Divergent mode (D). (j)–(l) Northwesterly wind regime (NW). A 15 day data gap in August 2013 is the reason for few regime estimates in that month.

in order to feed the transport in Barrow Canyon. This current pattern differs from the reversal regime, during which both the subsurface and surface flows were southwestward.

The fourth regime is the divergent mode (Figure 2d). North of 71.5°N, currents are ~10 cm s^{-1} and westward. South of this latitude, a recirculation is suggested, which includes cyclonic flow near the head of Barrow Canyon and an anticyclonic circulation at ~164°W, 70.5°N. The recirculation includes northeastward currents near the head of Barrow Canyon and southwestward currents in the southern mask between Icy Cape and Point Lay. Approximately 80% of the winds concurrent with the divergent mode are northeasterly, and ~70% of these winds have speeds >6 m s^{-1}, similar to those of the reversal regime; however, the subsurface and surface flow at BC2 is still northeastward, in contrast to the reversal regime. We will demonstrate that the divergent mode is a transitional stage between the northeastward-flowing and reversal regimes, as northeasterly winds begin to overcome the poleward pressure gradient.

As previously mentioned in section 2.3, SOM patterns vary slightly over the years; however, the regime descriptions above apply to all years. For example, the reversal regimes of 2010, 2011, 2013, and 2014 are all analogous to our description for the reversal regime in 2012. We find that the location of southwestward flow, offshore westward flow, and subsurface currents observed at BC2 approximate to the 2012 results. Similar agreements apply to the other three flow regimes.

Histograms show the monthly distribution of the four flow regimes for all years (Figure 3). The results indicate that the northwesterly wind regime was rare, consistent with the regional mean winds being predominantly from the east-northeast. The northeastward-flowing and reversal regimes occurred ~43% and ~27%

of the time, respectively. In general, as the frequency of the northeastward-flowing regime increases the frequency of the reversal pattern decreases, and vice-versa. The divergent mode appeared ~7% of the time overall with durations varying from several hours to a maximum of ~5 days.

The remaining pattern, not included in our categorization, consists of variable and weak (~1 cm s^{-1}) currents which are unreliable and occurred during periods of sparse data returns due to equipment maintenance, ice, ionospheric interference, and/or low winds. Collectively these conditions occurred ~14% of the time during 2012 and were aggregated into a pattern for data gaps referred to as G.

3.2. The Role of Winds: SOM Perspective

To illustrate how surface currents change under varying wind conditions, time series of the SOM regimes from August through October 2012, along with wind vectors, are presented in Figure 4 (see supporting
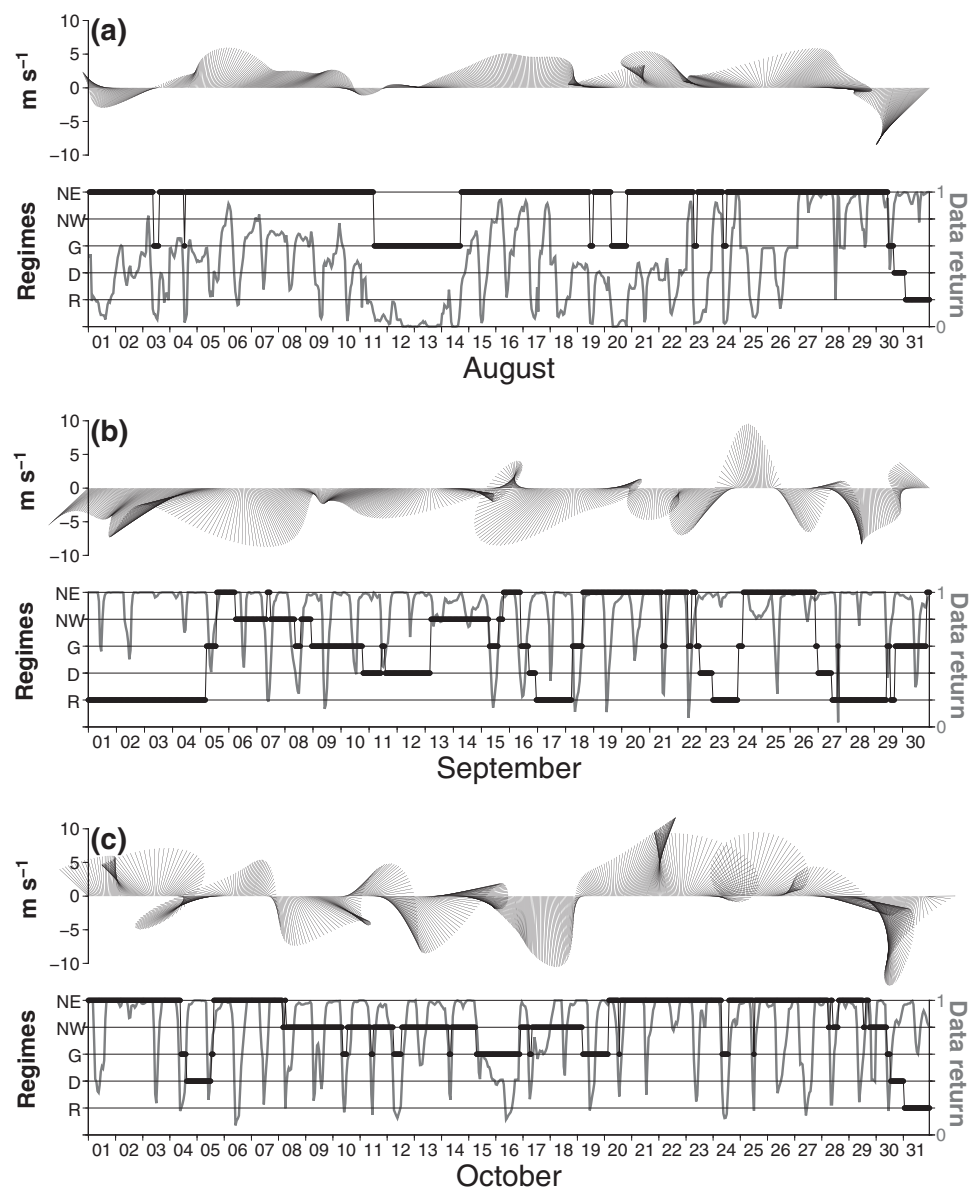
Figure 4. (top) (a) Time series of wind vectors in August 2012. The vector direction follows oceanographic convention. (bottom) SOM-derived circulation regimes (black dots) in August 2012 and normalized data returns (gray line). The abbreviations are: R, reversal regime; D, divergent mode; G, pattern G; NW, northwesterly wind regime; NE, northeastward-flowing regime. (b) As in Figure 4a, but for September 2012. (c) As in Figure 4a, but for October 2012.

information Figure S2). The gray line in Figure 4 tracks the normalized data return and facilitates interpretation of regimes associated with data gaps. For example, Pattern G occurred from 11 to 14 August when data returns were very low. Low data returns also occurred from 10 to 14 October due to diurnal ionospheric interference (Teague, 2001).

The wind field from 4 to 28 August was mainly southwesterly-southerly, and the northeastward-flowing regime persisted through most of the month. It was also present during the southerly wind events of 1–3, 6–7, and 20–28 October and occurred from 1–3 August and from 18–22 September when weak (≤ 4 m s^{-1}) winds from varying directions prevailed, consistent with our notion that weak winds are insufficient to overcome the poleward pressure gradient force.

After 28 August, southerly winds relaxed, and the winds became northeasterly and increased to a maximum of 10 m s^{-1} on 31 August. During this wind transition, the circulation shifted briefly into the divergent mode before the reversal regime was established. Reversal regimes consistently occurred during and/or shortly after pulses of strong (~ 10 m s^{-1}) northerly and/or northeasterly winds (e.g., 16–17, 22–23, and 27–29 September and 30–31 October). The divergent mode accompanied each transition from the northeastward-flowing regime to the reversal pattern, appearing as the northeasterly winds increased to relatively high magnitudes. Based on the wind time series and the EOF analysis of section 3.3, we find that the divergent mode occurred when northeasterly winds reached ~ 6 m s^{-1}. Hence, the divergent mode appears to be a transition between these two regimes; a point we will return to in section 4.

The northwesterly wind regime (Figure 2c) occurs primarily during periods when winds are veering from northwesterly to westerly or vice versa (e.g., 8–18 October) and/or during wind transitions involving westerlies (14–15 September). These results suggest that strong (>6 m s^{-1}) and sustained northwesterly winds (>1 day) are required to initiate this regime. We did not observe this pattern in 2011 and 2013, however, because northwesterly winds seldom occurred. When present, these events were short-lived (<1 day) in comparison to the >3 day events registered in 2012.

3.3. The Role of Winds: EOF Perspective

The bulk of the SOM patterns are the northeastward-flowing and reversal regimes, which suggests that these should be linked to the leading EOFs (Mau et al., 2007). In this section, we use EOFs and SOM patterns to corroborate one another.

Table 1 summarizes the EOF results in terms of the variance explained by the first (Mode 1) and second eigenmodes (Mode 2), the number of significant eigenmodes, and the correlation between PC1 of the currents and the winds. Mode 1 of the currents and winds account for at least 50% of the total variance, and the correlation between each variable's PC1 is significant. Mode 1 of the 2012 surface currents (Figure 5a) shows a pattern similar to the reversal regime derived from SOM (Figure 2b), which, when multiplied by its negative weight in the time domain, is analogous to the northeastward-flowing regime (Figure 2a). Mode 1 of the winds depicts northeasterlies (Figure 5c), and its negative weight describes southwesterly winds. The structures of Mode 1 in other years were similar to those in 2012, except in 2010 when Mode 1 for the winds was aligned in the east-west direction.

Table 1
Summary of the EOF Correlation Analysis From the Reconstructed Fields

Year	Months	Correlation coefficient between PC1 of currents and winds	# of significant eigenmodes (currents)	% variance explained by Mode 1 (currents, winds)	% variance explained by Mode 2 (currents, winds)
2010	9–10	0.36[a]	2	50, 63	17, 30
2011	8–10	0.56	1	65, 65	9, 27
2012	8–10	0.74	2	57, 57	11, 34
2013	9–10	0.75	3	66, 60	15, 29
2014	8–10	0.83	3	64, 75	14, 19

Note. The correlations are all significant at the 95% significance level using the effective number of degrees of freedom derived from the integral time scale.
[a]Low correlation coefficient is because wind Mode 1 in 2010 aligns nearly east-west, but Mode 1 of the currents is in the northeast-southwest direction.
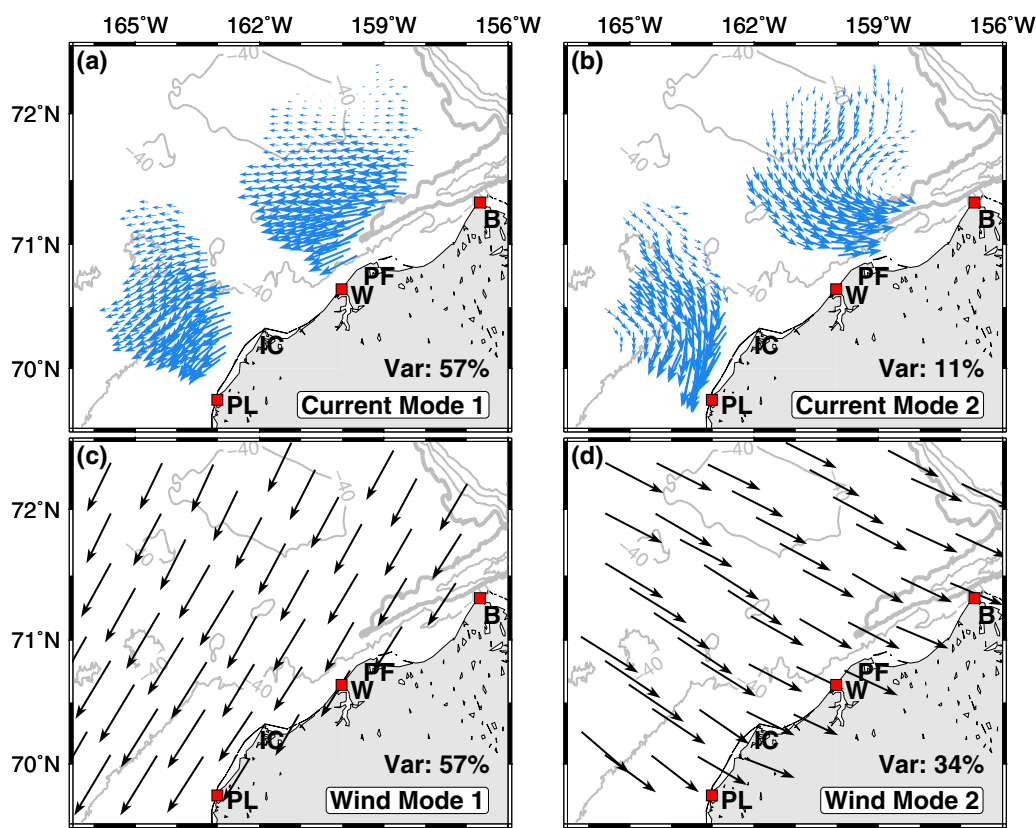
Figure 5. (a) EOF Mode 1 of 2012 reconstructed HFR data (blue vectors) and its explained variance. For clarity, only subsampled vectors are shown. (b) As in Figure 5a, but for Mode 2. (c) EOF Mode 1 of 2012 NARR winds (black vectors), also subsampled. (d) As in Figure 5c, but for Mode 2.

Mode 2 of the currents, which accounts for 9%–17% (depending upon year) of the surface current variance, is characterized by southward flows and onshore currents that appear to bifurcate somewhere between Icy Cape and Wainwright (Figure 5b). Meanwhile, Mode 2 of the winds portrays northwesterlies (Figure 5d) and explains 19%–34% of the variance across years. The structure of Mode 2 of the currents and winds in other years is comparable to those from 2012. The correlation between the principal components of Mode 2 (PC2) of the currents and the winds is only statistically significant for 2012 and 2014; however, as discussed later, we suspect that this relationship may not be meaningful.

Figure 6 shows the relationship between currents and winds in terms of wind speed and direction, PC1 of currents and winds, and the circulation regimes for the 2012 data. PC1 of currents and winds are normalized individually, and both are referenced to the reversal regime and northeasterly winds. PC1 values for the currents (winds) approaching unity indicate a flow field similar to that of Mode 1 (Figure 5a). In August, PC1 of the currents and winds were both generally negative (i.e., northeastward flow), consistent with the SOM results.

Northeasterly and northerly winds, as well as the divergent mode and reversal regime, were more frequent in September and October than in August. As a consequence, positive PC1 values for both the currents and winds were also more frequent. For example, the winds were northeasterly at $\sim$6 m s^{-1} throughout 10–13 September, when the pattern corresponded to the divergent mode (indicated by a red arrow, Figure 6). During this period, the current PC1 was $\sim$0.1, indicating the flow field had not yet fully reversed, consistent with the SOM analysis. Therefore, the EOF analysis corroborates the SOM conclusion that northeasterly winds $\geq$6 m s^{-1} are critical in shifting the surface circulation through the divergent mode and toward the reversal regime.

We examined four selected periods (labeled T1–T4, Figure 6) in September that consisted of reversal regimes. Periods T1–T3 had northeasterly winds >6 m s^{-1} (i.e., PC1 had values >0.5). Each event was
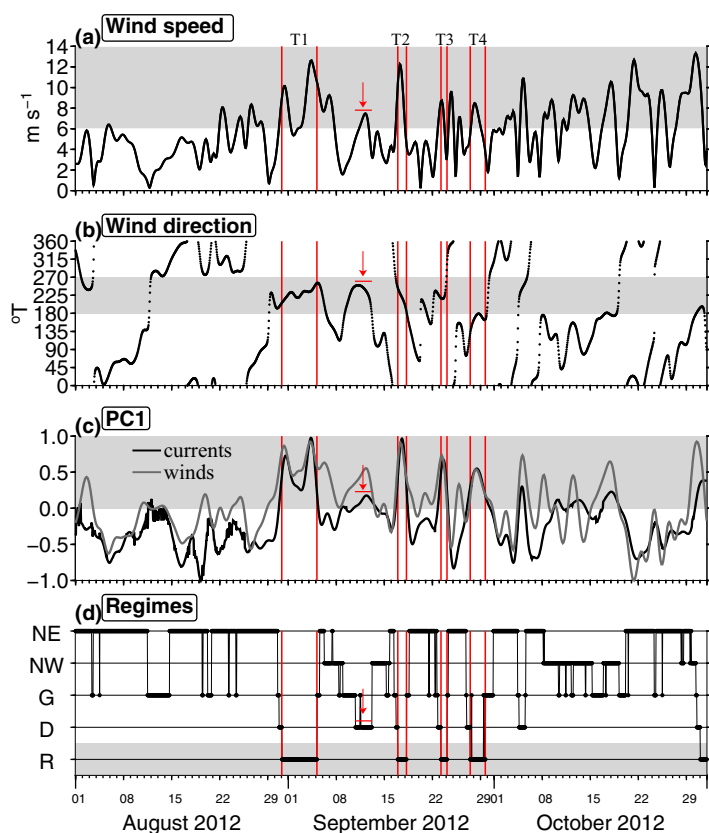
Figure 6. (a) Time series of wind speed with wind speeds ≥ 6 m s^{-1} highlighted in gray. (b) Time series of wind direction with gray shading corresponding to winds blowing from the northeast quadrant. (c) Time series of PC1 of surface currents (black) and PC1 of winds (gray) with gray-shaded areas highlighting positive PC1 values. PC1 values approaching one indicate currents or winds approximating the Mode 1 structure. (d) Time series of representative circulation regimes derived from SOM (black dots): R, reversal (highlighted in gray); D, divergent mode; G, pattern G; NW, northwesterly wind; NE, northeastward-flowing. The gray-shaded area highlights the reversal regime. Vertical red lines in each panel denote periods of selected reversal regimes (T1, T2, T3, and T4). Red arrow and bar denote a northeasterly wind event described in the text.

preceded by periods of weaker winds from varying directions. The current PC1 evolved similarly as its values changed from negative to positive. The temporal evolution of PC1 during each of these periods suggests that the reversals lagged the winds by 6–9 h. Period T4 also corresponded to the reversal regime, when winds were northerly with speeds >~6 m s^{-1}. Each of these reversals coincided with southwestward or upcanyon transports of ~1 Sv as measured by BC2 (Weingartner et al., 2017b).

The PC1 values for the currents fluctuate when the northwesterly wind regime is present (e.g., 9–18 October) but are comparatively small ($\leq \pm 0.2$). The northwesterly wind regime events are not well-described by the evolution of PC1 because their overall flow behaviors are different from those associated with Mode 1.

Unlike the good correspondence between the evolution of PC1 and the SOM-flow regimes, we do not find a direct relationship between PC2 and the flow regimes. For example, high positive PC2 (~0.8) for winds and currents were found in August, but the observed winds and flow fields were predominately southerly and northeastward, respectively. We suspect that EOF Mode 2 of winds and currents is a consequence of the orthogonality requirement of the EOFs computation and thus a limitation of EOFs. Our results suggest that higher-order eigenmodes should be interpreted cautiously for data sets containing large variability.

3.4. Mean Circulation Patterns

We formed composite circulation maps for periods when the HFR data recorded downcanyon (northeastward) and upcanyon (southwestward) flow events for 2010–2014. Primarily the classifications were defined by average flow conditions derived from twelve HFR grids (Figure 1b) near the head of Barrow Canyon. For the downcanyon condition flow is defined to be toward 56°T $\pm$ 4°, while for the upcanyon condition it is toward 236°T $\pm$ 4°, with 56°T the approximate axis of Barrow Canyon. Mean downcanyon and upcanyon patterns observed by HFR are comparable with the SOM-derived northeastward-flowing and reversal regimes, respectively.

For the 5 year period, we found 868 hourly surface current observations satisfying our downcanyon criterion. The polar histogram indicates that ~75% of the time the downcanyon pattern occurs under variable wind directions at moderate wind speeds (≤ 6 m s^{-1}). Approximately 25% of the winds were northeasterly (203–246°T), with only 5% of those >6 m s^{-1}. These strong northeasterlies are the catalyst for a reversal to upcanyon flow, and thus indicate when the flow field lagged the wind. The downcanyon average suggests four distinct flow regions (Figure 7a; labeled 1–4) under mean winds of ~1 m s^{-1} westward (~264°T). Region 1 lies north of 71.5°N on the eastern flank of Hanna Shoal, and here the mean currents are weak (a few cm s^{-1}) and directionally variable. The flow in Region 2 is generally eastward with mean currents 5–10 cm s^{-1}, consistent with results from moorings, ship-borne surveys, and models (Gong & Pickart, 2015; Spall, 2007; Weingartner et al., 2005; Winsor & Chapman, 2004). In the northwestern part of Region 2, the flow is southeastward, suggestive of flow moving eastward from the Central Channel across the shelf south of Hanna Shoal. Region 3 encompasses the head of Barrow Canyon, where mean currents are northeastward and swift (~30 cm s^{-1}). The mean currents in Region 4, which covers the southern portion of the southern radar mask, are northeastward at ~10 cm s^{-1}. The downcanyon average suggests convergence of the nearshore flow with that from the central shelf near 70.8°N, 162.5°W, with current speeds increasing as these flows converge.

Observations consistent with the upcanyon criterion were fewer, with only 368 hourly values. Mean winds for the upcanyon composite (Figure 7b) were ~7 m s^{-1} toward ~236°T, consistent with the reversal regime. Winds were ~70% northeasterly, ~6% northerly, and ~11% easterly. Overall the
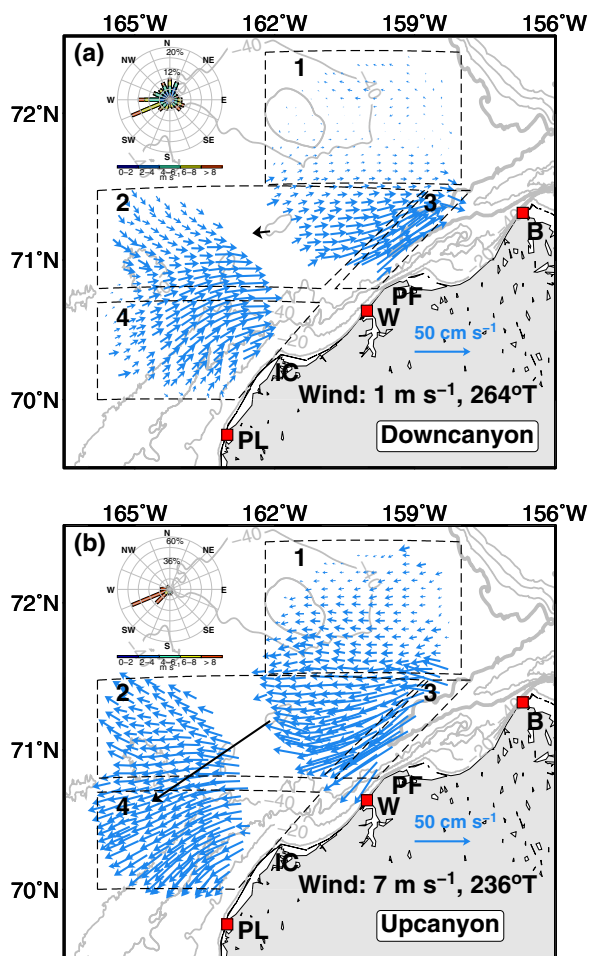
Figure 7. Mean (a) downcanyon and (b) upcanyon surface currents (blue vectors) for 2010–2014. Bathymetric contours (gray lines) are drawn within 200 m at 40 m intervals, with depths less than 40 m drawn at 10 m intervals. The black vector denotes the mean winds, and the polar histogram along 72°N denotes wind velocities. Areas circumscribed by dashed lines denote regions (labeled 1–4) of distinct flow behaviors (see text). For clarity, the vectors were subsampled.

currents are stronger than those of the downcanyon average. Surface currents in Region 1 are westward at ~9 cm s^{-1}, diminishing northward, while currents in Region 2 are westward or northwestward at 15–20 cm s^{-1}, which could carry canyon waters toward the south side of Hanna Shoal and across the central shelf. Currents near Barrow Canyon (Region 3) are particularly strong, with a mean of ~50 cm s^{-1} to the southwest (~240°T). The flow in Region 4 is also southwestward (~240°T) but with speeds of ~20 cm s^{-1}.

The composites indicate that the down and upcanyon flow structures in Regions 2 and 3 are mirror images of each other; however, Regions 1 and 4 are quite different from one another. For the upcanyon case, in Region 1 the flow is westward and oriented ~35° to the right of the wind. For the downcanyon case, the surface currents are weak and variable. We show later that the surface flow in Region 1 is consistent with Ekman dynamics.

For the Region 4 downcanyon case, the mean current speed is maximum (~25 cm s^{-1}) over the 40 m isobath and not statistically different ($p < 0.05$) from the speed over the 30 m isobath, but in the upcanyon case, the mean speeds along these isobaths are significantly different from one another. It is maximum (~38 cm s^{-1}) over the 30 m isobath and monotonically decreases offshore with the flow being ~32 cm s^{-1} over the 40 m isobath. These differences imply an asymmetry in the alongshore transport, with more transport carried by the inner shelf flow during upcanyon events compared to downcanyon cases. In the upcanyon case, the alongshore winds cause a sea level setdown and an alongshore southwestward flow established by the cross-shore pressure gradient. This gradient should be greatest within ~50 km of the coast, which is the e-folding scale for the 140 km barotropic radius of deformation (for a shelf depth of 40 m). In the downcanyon mean the winds are weak and directed offshore, in which case the mean flow is largely forced by the poleward pressure field and appears strongest over the 40 m isobath. This suggestion is consistent with the convergence in modeled streamlines shown by Winsor and Chapman (2004) and Spall (2007) for the same region.

3.5. Spatial Correlation Structure

In this section, we use the complex correlation function (Kundu & Allen, 1976) to examine the spatial correlation structure of the down and upcanyon flows using the DINEOF reconstructed data. The calculations use two reference grid points. The first, at 71.2°N, 160°W, is chosen to examine relationships between flow near Barrow Canyon and those elsewhere. The second grid point, at 72°N, 160°W, is over Hanna Shoal.
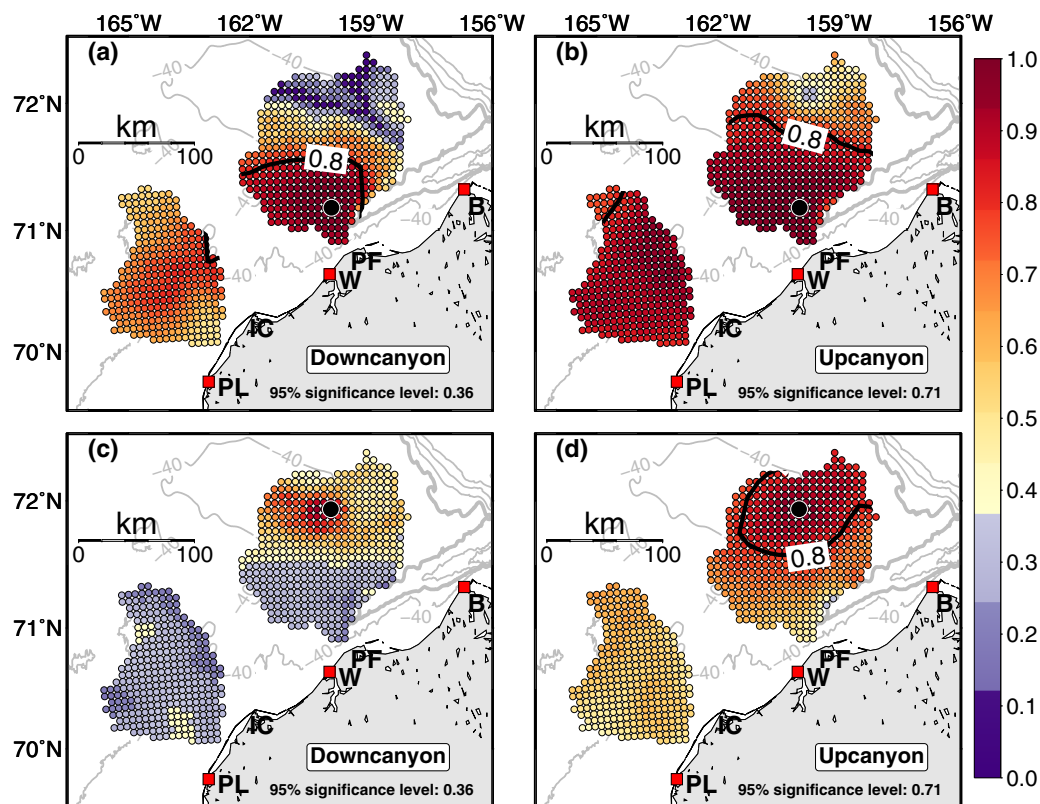
Based on the sample number (1148 for downcanyon; 249 for upcanyon) and estimated integral time scale (~40 h) from the 2012 DINEOF field, the 95% significance levels for the down and upcanyon correlations are 0.36 and 0.71, respectively. The correlation field using the Barrow Canyon grid point is similar for both flows (Figures 8a–8b), with correlations high in the canyon and across the southern mask but much smaller north of 71.5°N. The correlated regions are quite large. For example, the largest distance between grid points with correlations ≥ 0.8 is ~170 km for the downcanyon case and ~300 km for the upcanyon.

Using the Hanna Shoal grid point, the well-correlated region is limited to the area north of 71.5°N for the downcanyon case (Figure 8c). The length scale of the strongest correlation is only ~30 km, as expected given that the contributing currents are weak and variable in this region (Figure 7a). For the upcanyon case (Figure 8d), the spatial correlation structure is again significant and mainly confined to the region north of 71.5°N over a length scale of ~120 km. In aggregate, the SOM and the mean and correlation fields indicate that the shelf circulation north of 71.5°N is dynamically different from the shelf to the south.

Figure 8. Spatial distribution of complex correlations of surface currents with respect to a reference grid point (large black dot) for (a) and (c) downcanyon and (b) and (d) upcanyon flow. Black contour denotes the 0.8 correlation level. Correlation below the *e*-folding scale is shaded in cool colors. The 95% significance level is estimated from the effective number of degrees of freedom using the integral time scale.

4. Discussion

Our analyses have revealed two major surface circulation regimes related to the local winds. The northeastward-flowing regime transports water from along the coast and the central shelf into Barrow Canyon and toward the Arctic Ocean. During summer and early fall, this surface transport involves warm, low-salinity coastal waters, and somewhat more saline waters from the central shelf. The reversal regime transports waters up the canyon and across the Chukchi shelf, suggesting upwelling within the canyon and along the west coast of Alaska. We also identified the divergent mode, a transitional flow field established as northeasterly winds intensify, which eventually evolves into the reversal regime. This mode includes divergence in the nearshore currents between Icy Cape and Wainwright, with one branch leading into Barrow Canyon and the other proceeding southwestward. In addition, we found that the currents north of 71.5°N (Region 1 in Figure 7) are distinctly different from the currents south of this latitude. We explore these findings in greater detail in the following paragraphs.

In summer and fall, a portion of the Bering Strait inflow is carried eastward from the Central Channel and merges with ACC waters as they approach Barrow Canyon. This eastward flow is represented in circulation models forced solely by the poleward pressure gradient (Spall, 2007; Winsor & Chapman, 2004), in prior observations (Weingartner et al., 2005, 2013a), and is largely consistent with the northeastward-flowing regime (Figure 2a) and observed downcanyon mean (Figure 7a). The models also indicate that some of the Central Channel transport flows geostrophically around the north side of Hanna Shoal. Along the east side of the shoal the modeled flow is southward before turning eastward into the head of Barrow Canyon. This southward flow is much weaker than that on the western side because the isobaths diverge on the northeast side of the Shoal. However, the modeled southward flow is not captured by the SOM, nor is it evident in the vertically-averaged mean flows estimated from moorings on the shelf east of Hanna Shoal (Weingartner et al., 2017b).
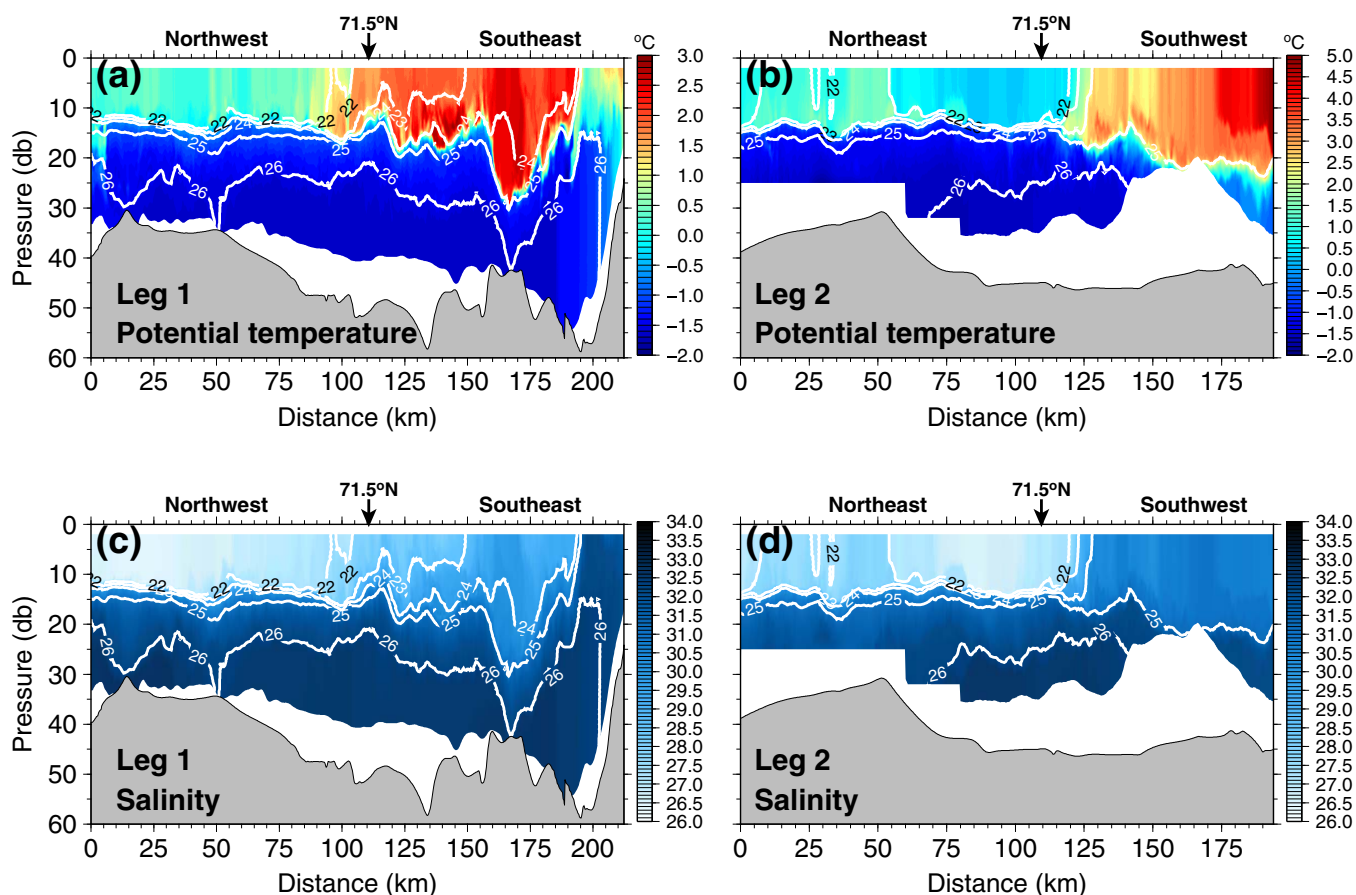
Figure 9. Vertical sections from September 2013 of potential temperature and salinity overlain with isopycnals (white contours) for (a) and (c) Leg 1 and (b) and (d) Leg 2. Black arrow denotes the location of 71.5°N. Note that the shading scales in Figures 9a and 9b and the horizontal scales for Legs 1 and 2 are different.

We believe that one cause in the differences in surface circulation north and south of 71.5°N lies with the shelf hydrographic structure. Figure 9 shows vertical sections of potential temperature (θ) and salinity (S) along Legs 1 and 2 (Figure 1) from September 2013. In both sections waters deeper than ∼20 m were cold (<−1°C) and salty (≥32.5) winter waters. North of 71.5°N, a ∼15 m deep surface layer contained cool (0°C) and fresh (salinity ∼26–29) meltwaters underlain by a thin but strong pycnocline. South of 71.5°N the stratification was weaker and the surface waters were warmer (3°C–5°C), moderately salty (salinity ∼31), and derived from Bering Sea summer waters. The front delineating these surface water masses was centered near 71.5°N. Similar fronts around this latitude are apparent in sections shown by Lu et al. (2015) and Weingartner et al. (2017a). The latter find that the shelf north of 71.5°N and east of Hanna Shoal supports a counterclockwise baroclinic geostrophic flow component that opposes the modeled barotropic flow around the Shoal. These opposing pressure tendencies result in weak geostrophic flow.

We suggest that the strong stratification north of 71.5°N in conjunction with weak geostrophic flow suggests that the surface currents in this region are largely governed by Ekman dynamics, with the Ekman layer presumably confined to the upper 15 m. For the upcanyon case, the mean winds were ∼7 m s^{-1} toward ∼236°T, which would impel a mean flow in the upper 15 m of ∼6 cm s^{-1} toward 326°T. The observed flow (within the upper 2 m) averaged 9 cm s^{-1} toward 270°T (i.e., ∼34° to the right of the wind). As discussed in Dzwonkowski et al. (2011), baroclinic shear and stratification inhibit deepening of the surface boundary layer and reduce its interaction with the bottom boundary layer, resulting in enhancement of surface transport. South of 71.5°N the stratification is weaker and the flow is primarily barotropic and geostrophic (Weingartner et al., 2013b), so that wind momentum is diffused over much of the water column.

We next examine the dynamics associated with the divergent mode aided by snapshots of wind and surface current maps (Figure 10) from September 2011. The maps encompass a period when the winds
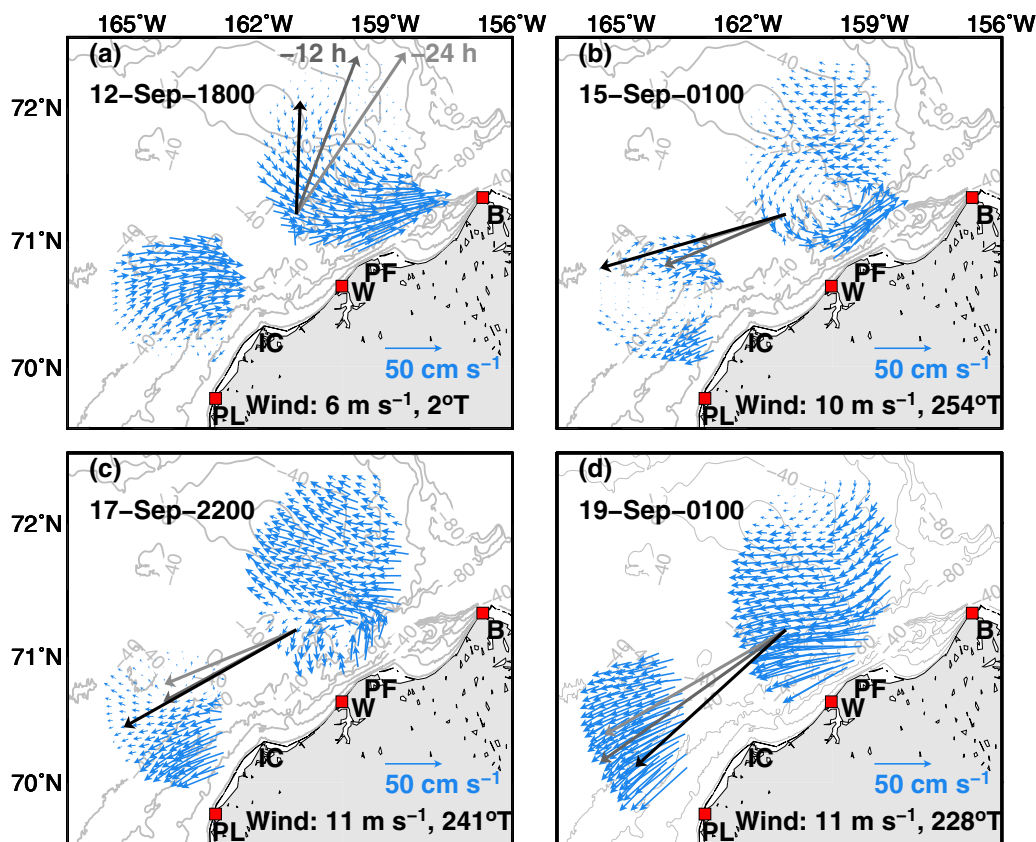
Figure 10. (a)–(d) HFR observations (blue vectors) during 12–19 September 2011 at indicated UTC time. The black vector denotes the wind at the cardinal hour of the snapshot, with the magnitude and direction shown in the legend, and the gray-shaded vectors are winds for the preceding 12 and 24 h. Bathymetric contours (gray lines) are drawn within 80 m at 10 m intervals. For clarity, the current vectors were subsampled.

transitioned from southerly (12 September, Figure 10a) to strong northeasterly (15–19 September, Figures 10b–10d). Each map includes a vector showing the wind at the measurement time (black) along with the wind vectors for the preceding 12 (dark gray) and 24 h (light gray).

Prior to 12 September the winds were southwesterly, and the northeastward-flowing regime held. At this time both the poleward pressure gradient and the coastal sea level setup acted in concert to propel the flow. On 13 September (not shown), the winds became east-northeasterly, and the divergent mode appeared for the next few days (Figure 10b). This transitional mode consisted of westward Ekman drift north of ∼71.5°N and southwestward alongshore flow inshore of the 30 m isobath offshore of Point Lay. The time scales for the appearance of these two circulation features is plausible. The Ekman adjustment time scale is only a few hours (Allen, 1973), whereas the spin-up time scale for the alongshore flow is proportional to h/r, where h is the water depth and r is the linear bottom friction coefficient. The adjustment to southwestward flow in the shallow (<30 m) nearshore waters should be ≤0.5 day for $r \sim 5 \times 10^{-4}$ m s^{-1} (e.g., Brink, 1998) but longer in deeper waters. Apparently, there is a ridge in the cross-shore pressure gradient northwest of Icy Cape near ∼70.5°N, manifested in the velocity field as the region of negligible flow along ∼70.5°N on 15 September (Figure 10b). Note that the width of the southwestward flow is ∼90 km and less than the local barotropic radius of deformation (∼130 km). The implication is that although the cross-shore sea level gradient sloped downward onshore, it was of insufficient magnitude to reverse the pressure gradient farther offshore or in Barrow Canyon. By 17 September (Figure 10c), the winds had veered more toward the southwest. In response, canyon waters offshore of Point Franklin began veering northward, while the area of southwestward flow between Icy Cape and Point Lay expanded offshore. The winds continued to veer toward the southwest and intensified such that by 19 September the reversal regime was fully established, with the swiftest flows in the canyon and along the coast (Figure 10d). The divergent

mode, although generally short-lived, thus has the potential to disperse materials advected from the central shelf along the coast of western Alaska and into Barrow Canyon.

We expect that the SOM-derived surface circulation patterns occur throughout the year and that the divergent mode should occur more frequently through late fall and winter when transitions between downcanyon and upcanyon flow events are more common (Weingartner et al., 2017b). However, threshold wind speeds that catalyze the changes amongst the various modes may differ given that the surface stress will be modulated by sea ice.

5. Summary

We used SOM and EOFs in an examination of HFR-derived surface current patterns in the northeastern Chukchi Sea during the open-water seasons (nominally August–October) from 2010 to 2014. We identified major surface current circulation patterns and their dynamics in conjunction with regional winds and showed how this portion of the shelf surface circulation responds to the wind field and a background poleward pressure gradient.

We found that surface currents south of $\sim71.5°$N and in Barrow Canyon flow northeastward except when northeasterly winds exceed ~6 m s^{-1}. The northeastward flow is primarily a manifestation of the large-scale pressure gradient between the Pacific and Arctic Oceans. When northeasterly wind speeds are >6 m s^{-1}, the coastal sea level setdown is large enough to cause southwestward surface flow inshore and westward flow over the central shelf. Less frequently southward surface currents occur over portions of the domain in response to northwesterly or westerly winds exceeding ~6 m s^{-1}.

We also detected the divergent mode, a transitional circulation feature of 1–5 days duration, which develops as the flow field adjusts from northeastward to southwestward in response to intensifying northeasterly winds. The divergent mode is characterized by eastward (onshore) flow across the central shelf, which diverges upon approaching the coast. A portion of this onshore flow continues into the head of Barrow Canyon while the remainder turns southwestward inshore of the 40 m isobath; however, sampling constraints prevented us from a precise determination of the nature of the divergence between these two regions. The divergent mode is a consequence of interaction amongst the poleward pressure gradient, increasing northeasterly winds ($> \sim6$ m s^{-1}), local bathymetry, and the regional hydrographic structure.

Along $\sim71.5°$N, there is an extensive zonally-oriented front. North of this front, surface pressure gradients are weak, and the surface currents are Ekman-like. The strong Ekman response occurs because the water column is strongly stratified; fresh, cool meltwaters occupy the upper 15 m, and cold, salty winter waters occupy the bottom layer. South of the front the manifestation of the poleward pressure gradient is stronger, and the water column is less stratified, with the surface layer containing moderately salty and warmer Bering Sea summer waters.

References

Aagaard, K., & Roach, A. T. (1990). Arctic ocean-shelf exchange: Measurements in Barrow Canyon. *Journal of Geophysical Research*, *95*(C10), 18163–18175. https://doi.org/10.1029/JC095iC10p18163

Aagaard, K., Weingartner, T. J., Danielson, S. L., Woodgate, R. A., Johnson, G. C., & Whitledge, T. E. (2006). Some controls on flow and salinity in Bering Strait. *Geophysical Research Letters*, *33*, L19602. https://doi.org/10.1029/2006GL026612

Allen, J. S. (1973). Upwelling and coastal jets in a continuously stratified ocean. *Journal of Physical Oceanography*, *3*(3), 245–257. https://doi.org/10.1175/1520-0485(1973)003<0245:UACJIA>2.0.CO;2

Barrick, D. E. (1978). HF radio oceanography: A review. *Boundary-Layer Meteorology*, *13*(1), 23–43. https://doi.org/10.1007/BF00913860

Beckers, J. M., & Rixen, M. (2003). EOF calculations and data filling from incomplete oceanographic datasets. *Journal of Atmospheric and Oceanic Technology*, *20*(12), 1839–1856. https://doi.org/10.1175/1520-0426(2003)020<1839:ECADFF>2.0.CO;2

Brink, K. H. (1998). Wind-driven currents over the continental shelf. In K. H. Brink & A. R. Robinson (Eds.), *The sea, Vol. 10: The global coastal ocean: Processes and methods* (Chapter 1, pp. 3–20). New York, NY: Wiley & Sons.

Chavanne, C., Janeković, I., Flament, P., Poulain, P.-M., Kuzmić, M., & Gurgel, K.-W. (2007). Tidal currents in the northwestern Adriatic: High-frequency radio observations and numerical model predictions. *Journal of Geophysical Research*, *112*, C03S21. https://doi.org/10.1029/2006JC003523

Danielson, S. L., Weingartner, T. J., Hedstrom, K. S., Aagaard, K., Woodgate, R., Curchitser, E., & Stabeno, P. J. (2014). Coupled wind-forced controls of the Bering–Chukchi shelf circulation and the Bering Strait throughflow: Ekman transport, continental shelf waves, and variations of the Pacific–Arctic sea surface height gradient. *Progress in Oceanography*, *125*, 40–61. https://doi.org/10.1016/j.pocean.2014.04.006

Dzwonkowski, B., Park, K., & Jiang, L. (2011). Subtidal across-shelf velocity structure and surface transport effectiveness on the Alabama shelf of the northeastern Gulf of Mexico. *Journal of Geophysical Research*, *116*, C10012. https://doi.org/10.1029/2011JC007188

Fang, Y.-C., Weingartner, T. J., Potter, R. A., Winsor, P. R., & Statscewich, H. (2015). Quality assessment of HF radar-derived surface currents using optimal interpolation. *Journal of Atmospheric and Oceanic Technology*, *32*(2), 282–296. https://doi.org/10.1175/JTECH-D-14-00109.1

Fredj, E., Roarty, H., Kohut, J., Smith, M., & Glenn, S. (2016). Gap filling of the coastal ocean surface currents from HFR data: Application to the mid-Atlantic bight HFR network. *Journal of Atmospheric and Oceanic Technology*, *33*(6), 1097–1111. https://doi.org/10.1175/JTECH-D-15-0056.1

Geoffroy, M., Majewski, A., LeBlanc, M., Gauthier, S., Walkusz, W., Reist, J. D., & Fortier, L. (2016). Vertical segregation of age-0 and age-1+ polar cod (*Boreogadus saida*) over the annual cycle in the Canadian Beaufort Sea. *Polar Biology*, *39*(6), 1023–1037. https://doi.org/10.1007/s00300-015-1811-z

Gong, D., & Pickart, R. S. (2015). Summertime circulation in the eastern Chukchi Sea. *Deep Sea Research Part II: Topical Studies in Oceanography*, *118*, 18–31. https://doi.org/10.1016/j.dsr2.2015.02.006

Hirano, D., Fukamachi, Y., Watanabe, E., Ohshima, K. I., Iwamoto, K., Mahoney, A. R., . . . Tamura, T. (2016). A wind-driven, hybrid latent and sensible heat coastal polynya off Barrow, Alaska. *Journal of Geophysical Research: Oceans*, *121*, 980–997. https://doi.org/10.1002/2015JC011318

Itoh, M., Nishino, S., Kawaguchi, Y., & Kikuchi, T. (2013). Barrow canyon volume, heat, and freshwater fluxes revealed by long-term mooring observations between 2000 and 2008. *Journal of Geophysical Research: Oceans*, *118*, 4363–4379. https://doi.org/10.1002/jgrc.20290

Johnson, W. R. (1989). Current response to wind in the Chukchi Sea: A regional coastal upwelling event. *Journal of Geophysical Research*, *94*(C2), 2057–2064. https://doi.org/10.1029/JC094iC02p02057

Kaihatu, J. M., Handler, R. A., Marmorino, G. O., & Shay, L. K. (1998). Empirical orthogonal function analysis of ocean surface currents using complex and real-vector methods. *Journal of Atmospheric and Oceanic Technology*, *15*(4), 927–941. https://doi.org/10.1175/1520-0426(1998)015<0927:EOFAOO>2.0.CO;2

Kaplan, D. M., & Lekien, F. (2007). Spatial interpolation and filtering of surface current data based on open-boundary modal analysis. *Journal of Geophysical Research*, *112*, C12007. https://doi.org/10.1029/2006JC003984

Kim, S. Y., Terrill, E., & Cornuelle, B. (2007). Objectively mapping HF radar-derived surface current data using measured and idealized data covariance matrices. *Journal of Geophysical Research*, *112*, C06021. https://doi.org/10.1029/2006JC003756

Kim, S. Y., Terrill, E. J., & Cornuelle, B. D. (2008). Mapping surface currents from HF radar radial velocity measurements using optimal interpolation. *Journal of Geophysical Research*, *113*, C10023. https://doi.org/10.1029/2007JC004244

Kohonen, T. (2001). *Self-organizing maps, Springer Series in Information Sciences* (3rd ed., Vol. 30, 501 pp.). New York, NY: Springer.

Kundu, P. K., & Allen, J. S. (1976). Some three-dimensional characteristics of low-frequency current fluctuations near the Oregon Coast. *Journal of Physical Oceanography*, *6*(2), 181–199. https://doi.org/10.1175/1520-0485(1976)006<0181:STDCOL>2.0.CO;2

Liu, Y., & Weisberg, R. H. (2005). Patterns of ocean current variability on the West Florida Shelf using the self-organizing map. *Journal of Geophysical Research*, *110*, C06003. https://doi.org/10.1029/2004JC002786

Liu, Y., Weisberg, R. H., & Mooers, C. N. K. (2006). Performance evaluation of the self-organizing map for feature extraction. *Journal of Geophysical Research*, *111*, C05018. https://doi.org/10.1029/2005JC003117.

Liu, Y., Weisberg, R. H., & Shay, L. K. (2007). Current patterns on the West Florida Shelf from joint Self-organizing map analyses of HF radar and ADCP data. *Journal of Atmospheric and Oceanic Technology*, *24*(4), 702–712. https://doi.org/10.1175/JTECH1999.1

Lu, K., Weingartner, T., Danielson, S., Winsor, P., Dobbins, E., Martini, K., & Statscewich, H. (2015). Lateral mixing across ice meltwater fronts of the Chukchi Sea shelf. *Geophysical Research Letters*, *42*, 6754–6761 https://doi.org/10.1002/2015GL064967

Martini, K. I., Stabeno, P. J., Ladd, C., Winsor, P., Weingartner, T. J., Mordy, C. W., & Eisner, L. B. (2016). Dependence of subsurface chlorophyll on seasonal water masses in the Chukchi Sea. *Journal of Geophysical Research: Oceans*, *121*, 1755–1770. https://doi.org/10.1002/2015JC011359

Mau, J.-C., Wang, D.-P., Ullman, D. S., & Codiga, D. L. (2007). Characterizing Long island sound outflows from HF radar using self-organizing maps. *Estuarine, Coastal and Shelf Science*, *74*(1–2), 155–165. https://doi.org/10.1016/j.ecss.2007.04.007

Mesinger, F., DiMego, G., Kalnay, E., Mitchell, K., Shafran, P. C., Ebisuzaki, W., . . . Shi, W. (2006). North American regional reanalysis. *Bulletin of the American Meteorological Society*, *87*(3), 343–360. https://doi.org/10.1175/BAMS-87-3-343

Mihanović, H., Cosoli, S., Vilibić, I., Ivanković, D., Dadić, V., & Gačić, M. (2011). Surface current patterns in the northern Adriatic extracted from high-frequency radar data using self-organizing map analysis. *Journal of Geophysical Research*, *116*, C08033. https://doi.org/10.1029/2011JC007104

Mountain, D. G., Coachman, L. K., & Aagaard, K. (1976). On the flow through Barrow Canyon. *Journal of Physical Oceanography*, *6*(4), 461–470. https://doi.org/10.1175/1520-0485(1976)006<0461:OTFTBC>2.0.CO;2

North, G. R., Bell, T. L., Cahalan, R. F., & Moeng, F. J. (1982). Sampling errors in the estimation of empirical orthogonal functions. *Monthly Weather Review*, *110*(7), 699–706. https://doi.org/10.1175/1520-0493(1982)110<0699:SEITEO>2.0.CO;2

Okkonen, S. R., Ashjian, C. J., Campbell, R. G., Maslowski, W., Clement-Kinney, J. L., & Potter, R. (2009). Intrusion of warm Bering/Chukchi waters onto the shelf in the western Beaufort Sea. *Journal of Geophysical Research*, *114*, C00A11. https://doi.org/10.1029/2008JC004870

Paduan, J. D., & Washburn, L. (2013). High-frequency radar observations of ocean surface currents. *Annual Review of Marine Science*, *5*, 115–136. https://doi.org/10.1146/annurev-marine-121211-172315

Paquette, R. G., & Bourke, R. H. (1974). Observations on the coastal current of arctic Alaska. *Journal of Marine Research*, *32*, 195–207.

Paquette, R. G., & Bourke, R. H. (1981). Ocean circulation and fronts as related to ice melt-back in the Chukchi Sea. *Journal of Geophysical Research*, *86*(C5), 4215–4230. https://doi.org/10.1029/JC086iC05p04215

Pickart, R. S., Moore, G. W. K., Mao, C., Bahr, F., Nobre, C., & Weingartner, T. J. (2016). Circulation of winter water on the Chukchi shelf in early Summer. *Deep Sea Research Part II: Topical Studies in Oceanography*, *130*, 56–75. https://doi.org/10.1016/j.dsr2.2016.05.001

Pickart, R. S., Pratt, L. J., Torres, D. J., Whitledge, T. E., Proshutinsky, A. Y., Aagaard, K., . . . Dail, H. J. (2010). Evolution and dynamics of the flow through Herald Canyon in the western Chukchi Sea. *Deep Sea Research Part II: Topical Studies in Oceanography*, *57*(1–2), 5–26. https://doi.org/10.1016/j.dsr2.2009.08.002

Questel, J. M., Clarke, C., & Hopcroft, R. R. (2013). Seasonal and interannual variation in the planktonic communities of the northeastern Chukchi Sea during the summer and early fall. *Continental Shelf Research*, *67*, 23–41. https://doi.org/10.1016/j.csr.2012.11.003

Richardson, A. J., Risien, C., & Shillington, F. A. (2003). Using self-organizing maps to identify patterns in satellite imagery. *Progress in Oceanography*, *59*(2–3), 223–239. https://doi.org/10.1016/j.pocean.2003.07.006

Roach, A. T., Aagaard, K., Pease, C. H., Salo, S. A., Weingartner, T., Pavlov, V., & Kulakov, M. (1995). Direct measurements of transport and water properties through the Bering Strait. *Journal of Geophysical Research*, *100*(C9), 18443–18457. https://doi.org/10.1029/95JC01673

Serreze, M. C., Barrett, A. P., Slater, A. G., Woodgate, R. A., Aagaard, K., Lammers, R. B., . . . Lee, C. M. (2006). The large-scale freshwater cycle of the Arctic. *Journal of Geophysical Research*, *111*, C11010. https://doi.org/10.1029/2005JC003424

Shimada, K., Kamoshida, T., Itoh, M., Nishino, S., Carmack, E., McLaughlin, F., . . . Proshutinsky, A. (2006). Pacific Ocean inflow: Influence on catastrophic reduction of sea ice cover in the Arctic Ocean. *Geophysical Research Letters*, *33*, L08605. https://doi.org/10.1029/2005GL025624

Spall, M. A. (2007). Circulation and water mass transformation in a model of the Chukchi Sea. *Journal of Geophysical Research*, *112*, C05025. https://doi.org/10.1029/2005JC003364

Steele, M., Ermold, W., & Zhang, J. (2008). Arctic ocean surface warming trends over the past 100 years. *Geophysical Research Letters*, *35*, L02614. https://doi.org/10.1029/2007GL031651

Stewart, R. H., & Joy, J. W. (1974). HF radio measurements of surface currents. *Deep Sea Research and Oceanographic Abstracts*, *21*, 1039–1049. https://doi.org/10.1016/0011-7471(74)90066-7

Stigebrandt, A. (1984). The north Pacific: A global-scale estuary. *Journal of Physical Oceanography*, *14*(2), 464–470. https://doi.org/10.1175/1520-0485(1984)014<0464:TNPAGS>2.0.CO;2

Taylor, M. H., Losch, M., Wenzel, M., & Schröter, J. (2013). On the sensitivity of field reconstruction and prediction using empirical orthogonal functions derived from Gappy data. *Journal of Climate*, *26*(22), 9194–9205. https://doi.org/10.1175/JCLI-D-13-00089.1

Teague, C. (2001). Ionospheric effects on coastal radar systems. In H. C. Graber & J. D. Paduan (Eds.), *Proceedings of the first radar oceanography international workshop* (pp. 56–61). Miami, FL: Rosenstiel School of Marine and Atmospheric Science, University of Miami.

Vilibić, I., Kalinić, H., Mihanović, H., Cosoli, S., Tudor, M., Žagar, N., & Jesenko, B. (2016). Sensitivity of HF radar-derived surface current self-organizing maps to various processing procedures and mesoscale wind forcing. *Computational Geosciences*, *20*(1), 115–131. https://doi.org/10.1007/s10596-015-9550-3

Weingartner, T. J., Aagaard, K., Woodgate, R., Danielson, S., Sasaki, Y., & Cavalieri, D. (2005). Circulation on the north central Chukchi Sea shelf. *Deep Sea Research Part II: Topical Studies in Oceanography*, *52*(24–26), 3150–3174. https://doi.org/10.1016/j.dsr2.2005.10.015

Weingartner, T. J., Cavalieri, D. J., Aagaard, K., & Sasaki, Y. (1998). Circulation, dense water formation, and outflow on the northeast Chukchi Shelf. *Journal of Geophysical Research*, *103*(C4), 7647–7661. https://doi.org/10.1029/98JC00374

Weingartner, T. J., Dobbins, E., Danielson, S., Winsor, P., Potter, R., & Statscewich, H. (2013a). Hydrographic variability over the northeastern Chukchi Sea shelf in summer-fall 2008–2010. *Continental Shelf Research*, *67*, 5–22. https://doi.org/10.1016/j.csr.2013.03.012

Weingartner, T. J., Fang, Y.-C., Winsor, P., Dobbins, E. L., Potter, R. A., Statscewich, H., . . . Borg, K. (2017a). The summer hydrographic structure of the Hanna Shoal region on the northeastern Chukchi Sea shelf: 2011–2013. *Deep Sea Research Part II: Topical Studies in Oceanography*, *144*, 6–20. http://doi.org/10.1016/j.dsr2.2017.08.006

Weingartner, T. J., Potter, R. A., Stoudt, C. A., Dobbins, E. L., Statscewich, H., Winsor, P. R., . . . Borg, K. (2017b). Transport and thermohaline variability in Barrow Canyon on the Northeastern Chukchi Sea Shelf. *Journal of Geophysical Research: Oceans*, *122*, 3565–3585. https://doi.org/10.1002/2016JC012636

Weingartner, T. J., Winsor, P., Potter, R. A., Statscewich, H., & Dobbins, E. L. (2013b). *OCS study BOEM 2012-079: Application of high frequency radar to potential hydrocarbon development areas in the Northeast Chukchi Sea*. (Final Rep., Reg. Contract M09AC15207, p. 162). Washington, DC: U.S. Department of Interior, Alaska Outer Continental Shelf. Retrieved from https://www.boem.gov/ESPIS/5/5265.pdf

Winsor, P., & Chapman, D. C. (2004). Pathways of Pacific water across the Chukchi Sea: A numerical model study. *Journal of Geophysical Research*, *109*, C03002. https://doi.org/10.1029/2003JC001962

Wood, K. R., Bond, N. A., Danielson, S. L., Overland, J. E., Salo, S. A., Stabeno, P. J., & Whitefield, J. (2015). A decade of environmental change in the Pacific Arctic region. *Progress in Oceanography*, *136*, 12–31. https://doi.org/10.1016/j.pocean.2015.05.005

Woodgate, R. A., Aagaard, K., & Weingartner, T. J. (2005). A year in the physical oceanography of the Chukchi Sea: Moored measurements from autumn 1990–1991. *Deep Sea Research Part II: Topical Studies in Oceanography*, *52*(24–26), 3116–3149. https://doi.org/10.1016/j.dsr2.2005.10.016

Woodgate, R. A., Aagaard, K., & Weingartner, T. J. (2006). Interannual changes in the Bering Strait fluxes of volume, heat and freshwater between 1991 and 2004. *Geophysical Research Letters*, *33*, L15609. https://doi.org/10.1029/2006GL026931

Woodgate, R. A., Weingartner, T. J., & Lindsay, R. (2012). Observed increases in Bering Strait oceanic fluxes from the Pacific to the Arctic from 2001 to 2011 and their impacts on the Arctic Ocean water column. *Geophysical Research Letters*, *39*, L24603. https://doi.org/10.1029/2012GL054092

Wyllie-Echeverria, T., Barber, W. E., & Wyllie-Echeverria, S. (1992). Water masses and transport of age-0 Arctic cod and age-0 Bering flounder into the northeastern Chukchi Sea. In J. B. Reynolds (Ed.), *Fish ecology in Arctic North America, American Fisheries Society Symposium* (Vol. 19, pp. 60–68). Bethesda, MD: American Fisheries Society.